Journal of Biomedical Optics

BiomedicalOptics.SPIEDigitalLibrary.org

Finesse of transparent tissue cutting by ultrafast lasers at various wavelengths

Jenny Wang
Georg Schuele
Daniel Palanker

SPIE.

Finesse of transparent tissue cutting by ultrafast lasers at various wavelengths

Jenny Wang,[a,*] Georg Schuele,[b] and Daniel Palanker[c,d]
[a]Stanford University, Department of Applied Physics, 452 Lomita Mall, Stanford, California 94305, United States
[b]Abbott Medical Optics, 1310 Moffett Park Drive, Sunnyvale, California 94089, United States
[c]Stanford University, Department of Ophthalmology, 452 Lomita Mall, Stanford, California 94305, United States
[d]Stanford University, Hansen Experimental Physics Laboratory, 452 Lomita Mall, Stanford, California 94305, United States

Abstract. Transparent ocular tissues, such as the cornea and crystalline lens, can be ablated or dissected using short-pulse lasers. In refractive and cataract surgeries, the cornea, lens, and lens capsule can be cut by producing dielectric breakdown in the focus of a near-infrared (IR) femtosecond laser, which results in explosive vaporization of the interstitial water, causing mechanical rupture of the surrounding tissue. Here, we compare the texture of edges of lens capsule cut by femtosecond lasers with IR and ultraviolet (UV) wavelengths and explore differences in interactions of these lasers with biological molecules. Scanning electron microscopy indicates that a 400-nm laser is capable of producing very smooth cut edges compared to 800 or 1030 nm at a similar focusing angle. Using gel electrophoresis and liquid chromatography/mass spectrometry, we observe laser-induced nonlinear breakdown of proteins and polypeptides by 400-nm femtosecond pulses above and below the dielectric breakdown threshold. On the other hand, 800-nm femtosecond lasers do not produce significant dissociation even above the threshold of dielectric breakdown. However, despite this additional interaction of UV femtosecond laser with proteins, we determine that efficient cutting requires plasma-mediated bubble formation and that remarkably smooth edges are the result of reduced thresholds and smaller focal volume. [DOI: 10.1117/1.JBO.20.12.125004]

Keywords: femtosecond laser surgery; photodissociation; protein; cavitation threshold; plasma-mediated; cataract surgery.

Paper 150604PR received Sep. 9, 2015; accepted for publication Nov. 19, 2015; published online Dec. 18, 2015.

1 Introduction

Short-pulse lasers have been invaluable tools in ophthalmic surgery since 1980, when nanosecond Nd:YAG infrared (IR) lasers were first introduced for posterior laser capsulotomy.[1] Since then, the two most prominent ophthalmic short-pulse laser systems are the argon fluoride (ArF) excimer laser for corneal ablation[2] and IR femtosecond lasers, first for creation of corneal flap in laser-assisted in-situ keratomileusis (LASIK),[3] and more recently for the dissection of cornea, lens, and lens capsule in cataract surgery.[4,5] These laser systems increase precision and reproducibility over mechanical tools or manual surgical procedures.

Along with the rapid adoption of surgical laser systems, there has been a growing understanding of the interaction mechanisms between lasers and tissue. ArF excimer laser ablation was originally believed to be a purely photochemical process, where absorption of high-energy photons ($E = 6.4\,\mathrm{eV}$) led to decomposition of molecular bonds and material ejection due to the increased volume of the photofragments.[6,7] This new mechanism was thought to explain the absence of thermal damage in surrounding tissue or polymer material. However, further research comparing ultraviolet (UV) and IR ablation revealed that these effects could also be explained by a photothermal mechanism, where the laser-material interaction was sufficiently confined.[8,9] The experimental results could be fit to both models[10] and it is now generally believed that 193-nm ablation involves a combination of the two.[11,12] For corneal ablation, Kitai et al.[13] showed that the quantum yield of photochemical bond-breaking is insufficient to explain ablation thresholds and argued that the thermally driven phase transition of water in the cornea is responsible for the remaining bond-breaking and material ejection.

Similarly, understanding of the plasma-mediated mechanism by which IR femtosecond lasers can deposit energy into water or transparent tissue has grown significantly.[11,14–16] Briefly, atoms are ionized through multiphoton or tunneling ionization within the focal zone of a high-intensity laser pulse. Free electrons can then absorb more photons through inverse-Bremsstrahlung absorption, gaining sufficient kinetic energy to ionize even more atoms during subsequent collisions. This "avalanche" ionization process results in a plasma that allows previously transparent tissues to absorb a significant amount of energy. Thermalization of this energy leads to rapid vaporization of the interstitial fluid, creating rapidly expanding cavitation bubbles which rupture the adjacent tissue.

The clinical success of excimer lasers and IR femtosecond lasers, as well as the growing understanding of laser-tissue interaction mechanisms, has spurred further interest in optimizing laser selection for surgery and in the search for new applications for existing systems. For corneal flap cutting, recent studies have introduced a 345-nm femtosecond laser[17–19] and 355-nm subnanosecond laser[20] for LASIK and a 1650-nm femtosecond laser for keratoplasty.[21] At the same time, IR femtosecond lasers have been used in the subcavitation regime for refractive index shaping[22,23] and for corneal cross-linking without photosensitizers.[24]

In this study, using scanning electron microscopy (SEM), we compare the structure and texture of the edges in cuts of the lens

*Address all correspondence to: Jenny Wang, E-mail: jywang2@stanford.edu

capsule produced by femtosecond lasers with the standard 1030-nm wavelength and two shorter wavelengths: 400 and 800 nm. Previous ultrastructural studies comparing manual capsulorhexis, the tearing of lens capsule with forceps, and capsulotomy with clinical laser systems[25,26] have demonstrated that edges of the laser-cut lens capsule have microgrooves that are not present in manually torn edges. These grooves become more prominent with increased pulse energy,[27,28] which is correlated with reduced capsular tear threshold[25] and can increase the risk of complications during phacoemulsification. Therefore, an increased finesse of the cut edges may be desirable for laser-assisted cataract surgery as well as in other tissue-cutting applications.

Our SEM results indicated that the 400-nm femtosecond laser is capable of producing dramatically smoother cuts than IR lasers. The low cutting threshold and lack of trapped residual air bubbles led us to investigate the interaction mechanisms aside from the classical plasma-mediated microexplosions. Recalling the debate about mechanisms of the excimer laser ablation, we assessed the contributions from multiphoton photochemical processes that affect the protein molecules of the lens capsule directly. First, we measured the photodissociation rate of proteins and polypeptides induced by femtosecond lasers and by an ArF excimer laser using gel electrophoresis and high-performance liquid chromatography (HPLC). Then, we compared the thresholds of cavitation and cutting of the lens capsule to determine the contributions of protein photodissociation and dielectric breakdown to laser surgery.

2 Materials and Methods

2.1 *Femtosecond Laser System*

A Ti:sapphire oscillator (Tsunami, Spectra-Physics) was used to seed a Nd:YLF-pumped (Merlin, Spectra-Physics) Ti:sapphire regenerative amplifier system (Spitfire, Spectra-Physics), which produced 800-nm, 150-fs pulses at 1 kHz. The 400-nm pulses were obtained via second-harmonic generation (SHG) with a 0.5-mm-thick beta barium borate (BBO) crystal. The duration of the 400-nm pulses was not measured, but given the moderate pump intensity, the durations should be comparable to the fundamental.[29] Several optical configurations were used in different parts of this experiment, as shown in Fig. 1.

2.1.1 *Lens capsule cutting*

For lens capsule cutting with 400-nm wavelength, two lenses in a Keplerian telescope configuration were used to expand the beam prior to delivery through a 10× microscope objective (Olympus Plan-FL). The laser beam under-filled the objective for a numerical aperture (NA) of ~0.1, as shown in Fig. 1(a), resulting in a theoretical focused $1/e^2$ beam waist diameter of 2.4 μm. Within the telescope, a half-waveplate and BBO crystal were used for SHG and variable attenuation of 400-nm output by rotating the polarization out of optimal phase matching. Two harmonic separator mirrors (CVI Melles Griot) were used to select the 400-nm wavelength and reject the 800-nm wavelength. A coaligned He-Ne laser and camera were used to position the lens sample at the proper focus. The sample stage was moved during laser cutting by two linear translation motors (Motor Mike, Oriel) driven by a custom LabView (National Instruments) program. Due to motor speed limitations, larger lateral spot spacing was obtained by dividing the laser repetition rate down, as low as 20 Hz, when needed. Spacing could be varied between 0.1 and 2 μm. Vertical translation occurred between each complete horizontal scan and varied between 4 and 10 μm. Pulse energy was measured with a power meter (PE9, Ophir Optronics) and ranged from 20 to 2000 nJ.

For lens capsule cutting with 800-nm wavelength, a similar setup was used. The SHG crystal was removed and a polarizing beam splitter was used instead as a variable attenuator. Silver mirrors replaced the harmonic separators for steering the beam into the 10× objective at an NA of 0.12, resulting in a calculated minimum focused $1/e^2$ beam waist diameter of 4.2 μm. During cutting, pulse energy varied from 0.3 to 2 μJ and lateral spacing varied from 0.1 to 2 μm. Vertical steps were performed after each complete horizontal scan and varied between 4 and 10 μm. For only the evaluation of edge quality while changing spot density, longer laser pulses (1.6 ps, 800 nm) were used. Lens capsule cutting with longer pulses was done with the optical layout

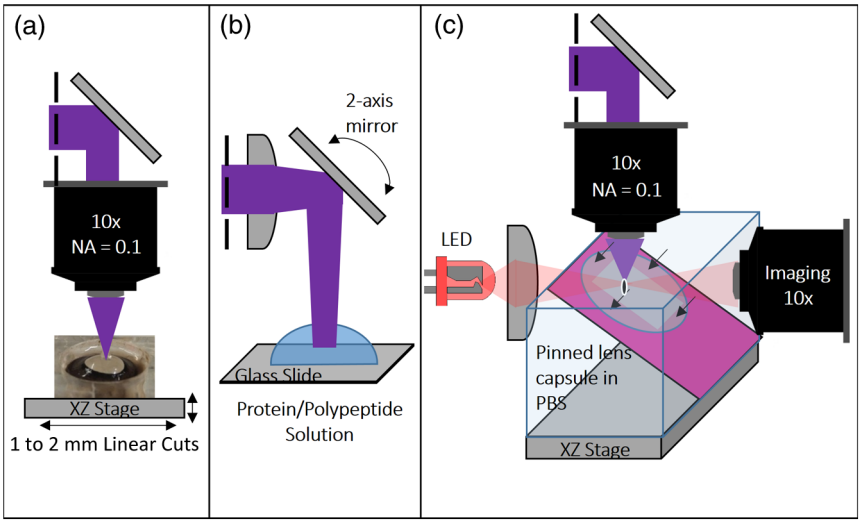

Fig. 1 Summary of laser setups: (a) lens capsule cutting on intact lens through 10× objective; (b) scanned irradiation of protein and polypeptide solution; and (c) laser delivery and imaging for cavitation bubble detection in extracted lens capsule.

previously described for 150-fs pulses and pulse energy of 16.3 μJ, fixed vertical spacing of 10 μm, and lateral spacing varying from 0.2 to 20 μm.

For comparison with a clinical 1030-nm femtosecond laser, we used a CATALYS® Precision Laser System (Abbott Medical Optics) with sub-600-fs pulse duration and NA of approximately 0.1. During cutting, a 5-mm capsulotomy was created using pulse energies of 5 or 10 μJ with lateral spacing of 5 or 10 μm, respectively, and vertical spacing of 10 μm.

2.1.2 *Photodissociation experiments*

For protein and polypeptide photodissociation experiments, the setup was simplified by removing the telescope (for 800 nm) or converting to a relay (for 400 nm), and replacing the 10× objective with a singlet lens ($f = 200$ mm) for NA of 0.014. A scanning mirror (optics in motion) was used to scan the loosely focused beam through the protein or polypeptide solution that rested on a microscope slide, as shown in Fig. 1(b). The scanning mirror was controlled via a custom LabView (National Instruments) program to scan over the entire area of the fluid sample for the desired number of scans.

2.1.3 *Cavitation bubble thresholds*

Cavitation bubble thresholds in distilled water and in protein solution were measured with a previously described flash photography setup with light-emitting diode (LED) illumination,[30] where bubbles were detected as shadows. The laser delivery system was the same as described for lens capsule cutting in Sec. 2.1.1, except that the focus was in bulk liquid rather than on the surface of a porcine lens. Different solutions of bovine serum albumin (BSA) from 0.5 to 10 mg/mL were used to measure the effect of protein concentration on 400- and 800-nm thresholds. A pressure transducer (VP-1093, CTS Valpey Corporation) was also positioned within the cuvette to detect bubbles acoustically. Signals were amplified (SRS560, Stanford Research Systems) and viewed on an oscilloscope to detect bubble formation.

Cavitation bubble formation in the lens capsule rather than liquid was also measured using this flash photography system, as shown in Fig. 1(c). The lens was extracted from a pig eye and the anterior capsule was cutoff and pinned to a wax frame oriented at 45 deg to the laser beam axis as well as the imaging axis. This allowed simultaneous laser cutting and imaging of the resulting cavitation bubble formed in the transparent tissue. The sample cuvette was filled with saline during the measurements and cavitation bubbles were detected as shadows blocking the LED illumination in the resulting images.

After determining the bubble threshold in the lens capsule, a continuous cut was attempted at pulse energies slightly below or above the bubble threshold with very tight lateral spot spacing of 0.2 μm and axial spacing of 4 μm. Samples were imaged during cutting using continuous LED illumination to check for residual gas buildup. After laser delivery, forceps were used to gently probe the sample to determine if a complete cut was made. If so, cut edges were separated and analyzed with SEM.

2.2 *Excimer Laser System*

An ArF excimer laser (OPTex, Lambda Physik), producing 193-nm, 8-ns pulses, was used to irradiate protein and polypeptide solution for photodissociation experiments. A diverging CaF_2 lens was used to expand the beam area to cover the sample volume and an iris was used to define the irradiation area. The sample liquid was sandwiched between two quartz (fused silica) windows spaced with #1 coverslips. The incident pulse energy was measured with a pyroelectric energy sensor (PE-25BB, Ophir Optronics) and converted into fluence. To assess the nonlinearity of the photodissociation of protein and polypeptide, a constant total energy was delivered to the sample, while varying the pulse energy and total number of pulses.

2.3 *Lens Capsule Cut Edge Imaging*

Pig eyes (First Vision Tech, Sunnyvale, Texas) were obtained from an abattoir and shipped overnight on ice. For comparison to manual cataract surgery, a ~4-mm open-sky capsulorhexis was performed. For 400- and 800-nm laser cutting, lenses were carefully extracted from the eye without puncturing the lens capsule and stored in balanced salt solution at 4°C until use. Lenses were used within 48 h of extraction. To reduce drying during laser cutting, lenses were held in a plastic sample holder with a saline reservoir beneath. The top surface of the lens capsule was exposed to air during cutting of straight lines between 2 and 4 mm in length. For 1030-nm laser cutting, only the cornea was removed prior to a 5-mm laser capsulotomy using a CATALYS (Abbott Medical Optics) system. After laser cutting in all cases, the anterior lens capsule with laser cuts was removed from the lens, pinned to dental wax, and fixed in 1.25% gluteraldehyde. This helped prevent obscuring of the cut edge by extruding lens material or by folding of the capsule during sample processing. After a minimum of 24 h of fixation at room temperature, samples were processed as follows: 0.1-M sodium cacodylate rinse (30 min), osmium tetraoxide postfixation (1 h), 30% ethanol, 50% ethanol, 70% ethanol, 90% ethanol, and 2× 100% ethanol (20 min each). Samples were then critical point dried and sputter coated with 10 nm of Au/Pd before imaging by SEM (Hitachi S-3400N VP-SEM, Stanford Cell Sciences Imaging Facility).

2.4 *Protein Breakdown Analysis*

BSA was used as a common soluble protein of definite length (583 amino acids, 66.5 kDa) that could be analyzed after laser irradiation with gel electrophoresis. BSA was dissolved in water to a concentration of 1 mg/mL and irradiated by the different lasers described earlier. After irradiation, 10 μL was collected and processed for gel electrophoresis using the Criterion XT system (Bio-Rad) according to the manufacturer's protocol. For each gel, a control sample was placed on the sample surface but not irradiated before collection. The gel was stained with Coomassie Blue R-250 for 1 h and destained (40% methanol, 10% acetic acid) until the background gel was clear. Gels were placed on a lightbox and images were captured with a digital camera.

2.5 *Polypeptide Breakdown*

A short, water-soluble, commercially available polypeptide was chosen to observe laser breakdown products using high-performance liquid chromatography/mass spectrometry (HPLC/MS) with the sequence Trp-His-Trp-Leu-Gln-Leu (WHWLQL) with 882 molecular weight. The polypeptide was dissolved in water and diluted to 0.1 mg/mL for laser irradiation. After irradiation, 5 μL were collected and analyzed using a Waters 2795 HPLC

with Micromass ZQ single quadrupole mass spectrometer (Vincent Coates Foundation Mass Spectrometry Laboratory). Mass spectrogram data were then analyzed using MassLynx (Waters Corp.) software.

3 Results

3.1 *Edge of the Lens Capsule Cut*

Intact porcine lens capsules were cut with 400- and 800-nm femtosecond lasers using the same focusing angle (NA 0.1). First, the same spot spacing (2 μm lateral and 10 μm vertical) was used to make 2- to 4-mm linear cuts while decreasing pulse energy until the lens capsule no longer splits. The minimum pulse energies were 0.75 μJ for 800 nm and 0.25 μJ for 400 nm. Then, the spot density was increased in order to determine the minimum pulse energy capable of cutting the lens capsule. For the 800-nm femtosecond laser, a complete cut could be made with a pulse energy of 0.6 μJ and spot spacing of 1.5 μm laterally and 10 μm vertically. Further increases in spot density did not allow for lower pulse energies. Using the same process, we found that the 400-nm femtosecond laser was capable of making cuts with only 20-nJ pulse energy, although it required very dense spot spacing of 0.1 μm laterally and 4 μm vertically. Intriguingly, there were no visible bubbles during cutting, and this pulse energy is below the threshold of cavitation bubble formation in water and protein solution, as described in Sec. 3.2.

The resulting lens capsule edges were imaged with SEM and are shown in Fig. 2. The manually torn lens capsule [Fig. 2(a)] has a remarkably smooth edge with fibers that run along the edge of the tear. In contrast, a porcine lens capsule cut using the CATALYS (Abbott Medical Optics) laser system [Fig. 2(b)] at highest pulse energy (10 μJ) shows clear grooves along the laser beam direction and perpendicular to the capsule surface. Lens capsule cut with the 800-nm femtosecond laser [Fig. 2(c)] at the minimum pulse energy is qualitatively similar, with clear laser grooves but narrower and much closer spaced. Unlike the other two laser cuts, the 400-nm femtosecond laser can produce a very smooth lens capsule edge when operated at or near its minimum pulse energy for cutting. As shown in Fig. 2(d), the edge is more similar to the manually torn capsule in smoothness. However, the orientation of the surface texture is along the laser direction rather than the capsule surface, confirming that the capsule is split by laser-induced plasma formation rather than tearing.

To explore the effect of spot spacing on edge smoothness, we made lens capsule cuts with high-energy pulses (16.3 μJ, $\lambda = 800$ nm, $\tau = 1.6$ ps) at constant vertical spacing of 10 μm, while changing the lateral spot spacing from 1 to 10 μm. The resulting edges imaged with SEM are shown in Fig. 3. Cutting with 10-μm spot spacing produces an edge with regular laser grooves, as shown in Fig. 3(a), while increasing the spot density by a factor of 10 [Fig. 3(b)] results in an irregular, messy edge.

3.2 *Bubble Thresholds in Water and in Protein Solution*

Cavitation bubble thresholds were measured with flash imaging and acoustic detection. In general, visible shadowing of LED illumination proved slightly more sensitive to bubbles than acoustic detection in our geometry and determined the minimum threshold. For each pulse energy step, 20 pulses were recorded and the existence of a bubble or no bubble was noted. The resulting probabilities of bubble formation were fit with probit regression and the threshold was determined to be the energy value

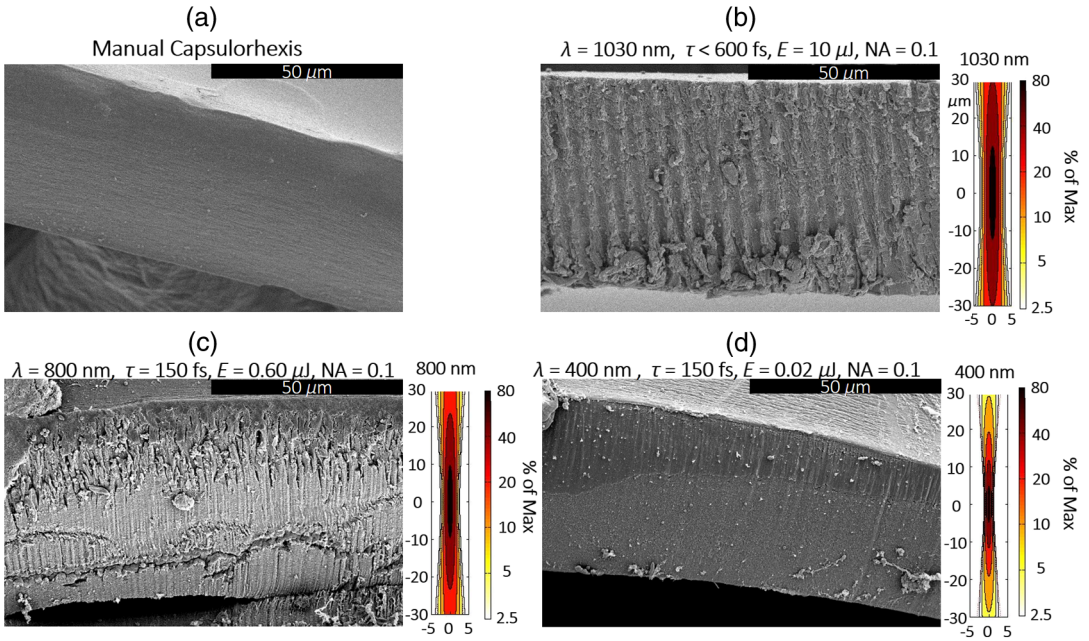

Fig. 2 Scanning electron micrographs (SEM) of porcine lens capsule edges after (a) manual capsulorhexis, (b) laser capsulotomy with CATALYS® system with 10-μJ pulse energy and 10 μm lateral and 10 μm vertical spacing, (c) laser capsulotomy with 800-nm, 150-fs pulses focused at NA of 0.1 with pulse energy of 0.6 μJ, and 1.5 μm lateral and 4 μm vertical spacing, and (d) laser capsulotomy with 400-nm, 150-fs pulses focused at NA of 0.1 with pulse energy of 20 nJ and 0.1 μm lateral and 4 μm vertical spacing. Corresponding contour plot of energy distribution for an ideal Gaussian beam at numerical aperture of 0.1 is shown at right for each laser wavelength.

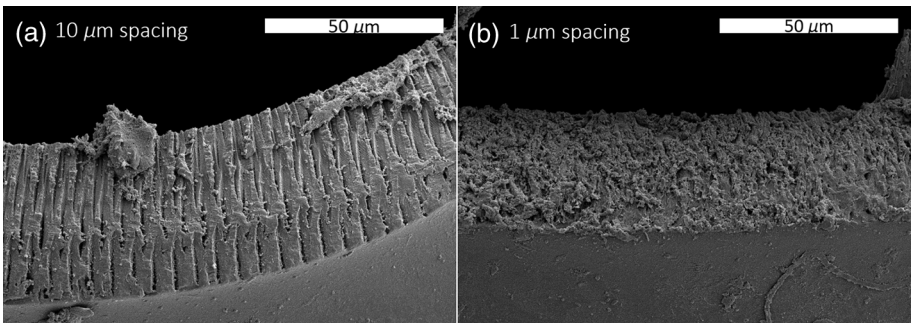

Fig. 3 SEM of 800 nm, 1.6 ps laser cuts in porcine lens capsule with pulse energy of 16.3 μJ, constant vertical spacing of 10 μm, and lateral spot spacing of (a) 10 μm and (b) 1 μm.

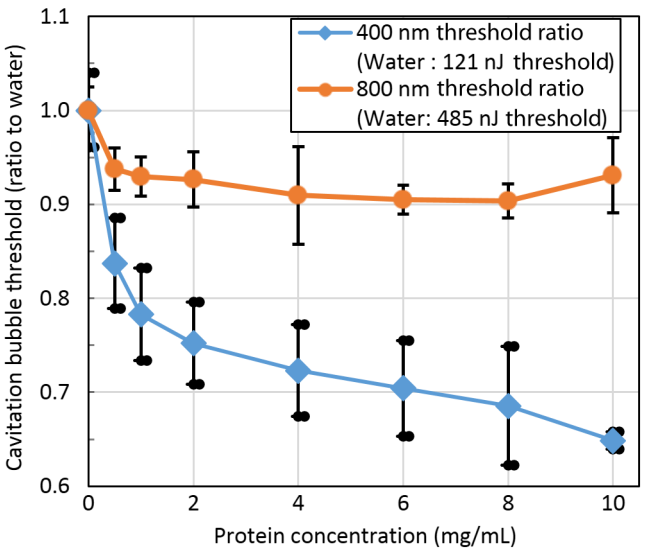

Fig. 4 Cavitation bubble threshold plot for 400- and 800-nm femtosecond lasers at various concentrations of bovine serum albumin (BSA) solution.

where cavitation bubbles are expected to form 50% of the time. The results of this analysis for distilled water and protein solutions are shown in Fig. 4, with error bars corresponding to 10th and 90th percentiles of the bubble formation.

For 400 nm, the bubble threshold in distilled water was 121 nJ, and the addition of BSA significantly decreased the cavitation bubble threshold. At 10 mg/mL of BSA, the threshold is reduced by 34%. In contrast, bubble thresholds for 800 nm are only slightly reduced by addition of protein—no more than 7% —from the threshold in distilled water of 485 nJ.

3.3 *Photodissociation of Protein and Polypeptide*

Gel electrophoresis was used to detect laser-induced dissociation of BSA by measuring the amount of intact protein that survives laser irradiation. For 800-nm femtosecond pulses, we use a loosely focused beam that is scanned over a drop of BSA solution (1 mg/mL) at energies at or slightly below the dielectric breakdown (cavitation bubble) threshold as determined by the appearance of visible bubbles. The resulting gel in Fig. 5(a) shows that 800-nm radiation, even when cavitation bubbles are produced and the scanning is repeated four times, does not dissociate the protein.

In contrast, the 400-nm femtosecond pulses are capable of inducing protein dissociation, even at pulse energies below the threshold of cavitation. As can be seen in Fig. 5(b), the effect is intensity dependent: focused beam breaks down most of the protein in solution at 33% and 66% of the bubble threshold. However, an unfocused beam of the same energy produces no dissociation. This is contrasted with the 193-nm excimer laser, where photodissociation is linear: it occurs at the same rate regardless the variation of the beam intensity, as long as the constant total energy is maintained. As shown in Fig. 5(c), the excimer laser breaks down between 50% and 70% of the protein at these settings.

We also used HPLC/MS to measure the amount of intact polypeptide (Trp-His-Trp-Leu-Gln-Leu) after laser-induced photodissociation by integrating the peak in the channel for a mass-to-charge (m/z) ratio of 883, which represents the intact ion. To determine whether the effect is linear or multiphoton, we varied the number of pulses and pulse energy, while maintaining the total delivered energy. The thresholds of bubble formation in polypeptide solution with the loosely focused beam (NA 0.014) were 20 and 5 μJ for 800 and 400 nm, respectively, as determined by appearance of bubbles. Figure 6(a) shows the effect for 400- and 800-nm femtosecond laser irradiation. At 10 μJ, half the cavitation bubble threshold for 800 nm, laser irradiation shows a negligible effect on the amount of intact polypeptide. Increasing the pulse energy to the cavitation threshold or twice the cavitation threshold produces a slight effect with 92% and 87% of the polypeptide remaining, respectively. The effect is much more robust with 400-nm femtosecond pulses, where 10-μJ pulses, twice the cavitation bubble threshold, leaves only 33% of the polypeptide remaining. The effect persists even below the cavitation bubble threshold where 2.5-μJ pulses (half the cavitation threshold) leave 70% of the polypeptide intact. In contrast, the excimer laser effect is robust and linear for the entire range of pulse energy densities, as shown in Fig. 6(b).

As for the products of small polypeptide dissociation with excimer laser irradiation, we were able to identify two photoproducts broken apparently along the peptide backbone, the B_2 and Z_4 fragments shown in Fig. 7(a). The appearance of products corresponding to these mass fragments after excimer laser irradiation is shown in Figs. 7(b) and 7(c) as earlier peaks in the chromatogram, pointed to by the arrows. In 400-nm irradiation, these photoproducts were minimal even though

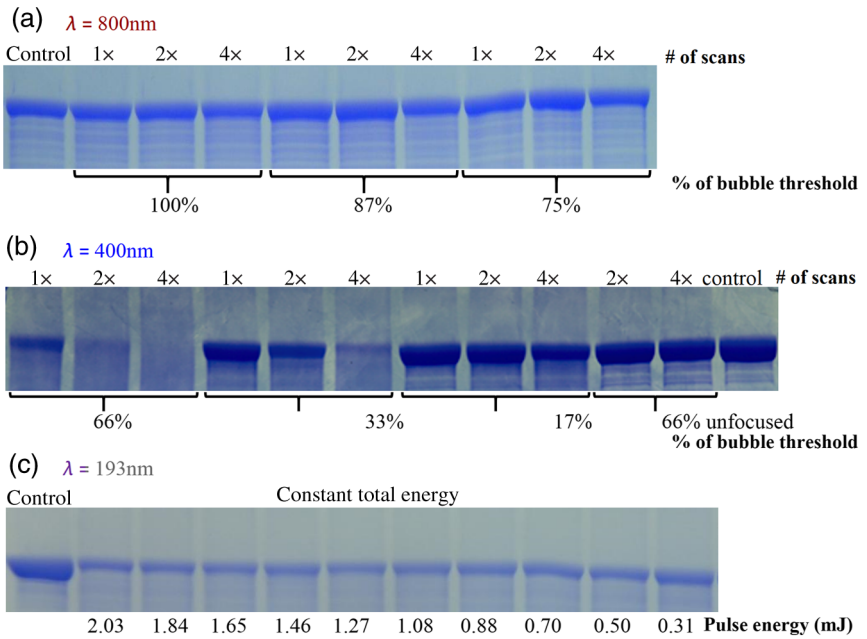

Fig. 5 Gel electrophoresis showing intact BSA protein band remaining after laser irradiation with (a) 800-nm femtosecond, (b) 400-nm femtosecond, and (c) 193-nm excimer laser.

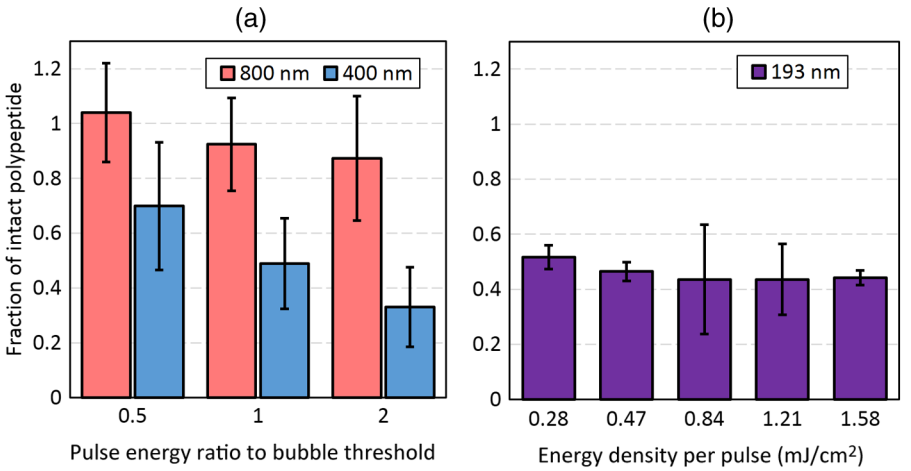

Fig. 6 Bar charts showing fraction of intact polypeptide (WHWLQL) remaining after laser irradiation measured by integration of 883 m/z signal from high-performance liquid chromatography/mass spectrometry. The number of pulses was decreased to keep total delivered energy constant for each wavelength. (a) Comparison of 800- and 400-nm femtosecond lasers and (b) 193-nm excimer laser.

polypeptide breakdown did occur, as seen in Figs. 7(d) and 7(e), respectively, and no other clear ions were detected.

3.4 *Lens Capsule Cutting with Cavitation Bubble Detection*

An example of cavitation bubble detection for a 400-nm femtosecond laser in porcine lens capsule is shown on the left side in Fig. 8. Bubbles forming in phosphate buffered saline are shown on the right side for comparison. All images were captured 0.5 μs after the laser pulse arrived. The shadow indicates the presence of a cavitation bubble. Cavitation threshold energies varied quite a bit (48 to 108 nJ) most likely due to tissue sample variations. As such, the cavitation threshold energy had to be determined for each lens capsule to serve as the reference point for the cutting threshold in that sample. Since bubble formation within the capsule resulted in permanent craters, as indicated by the red arrows, the sample was translated 50 μm laterally between pulses and the threshold was determined by decreasing the pulse energy until no bubble was visible.

After the bubble threshold in the lens capsule sample was determined, a continuous cut was attempted. Figure 9 shows three examples of the results with the 400-nm femtosecond laser at different pulse energies: 600 nJ, well above the bubble threshold; 60 nJ, at the bubble threshold; and 42 nJ, below the bubble threshold, with corresponding SEM images in the

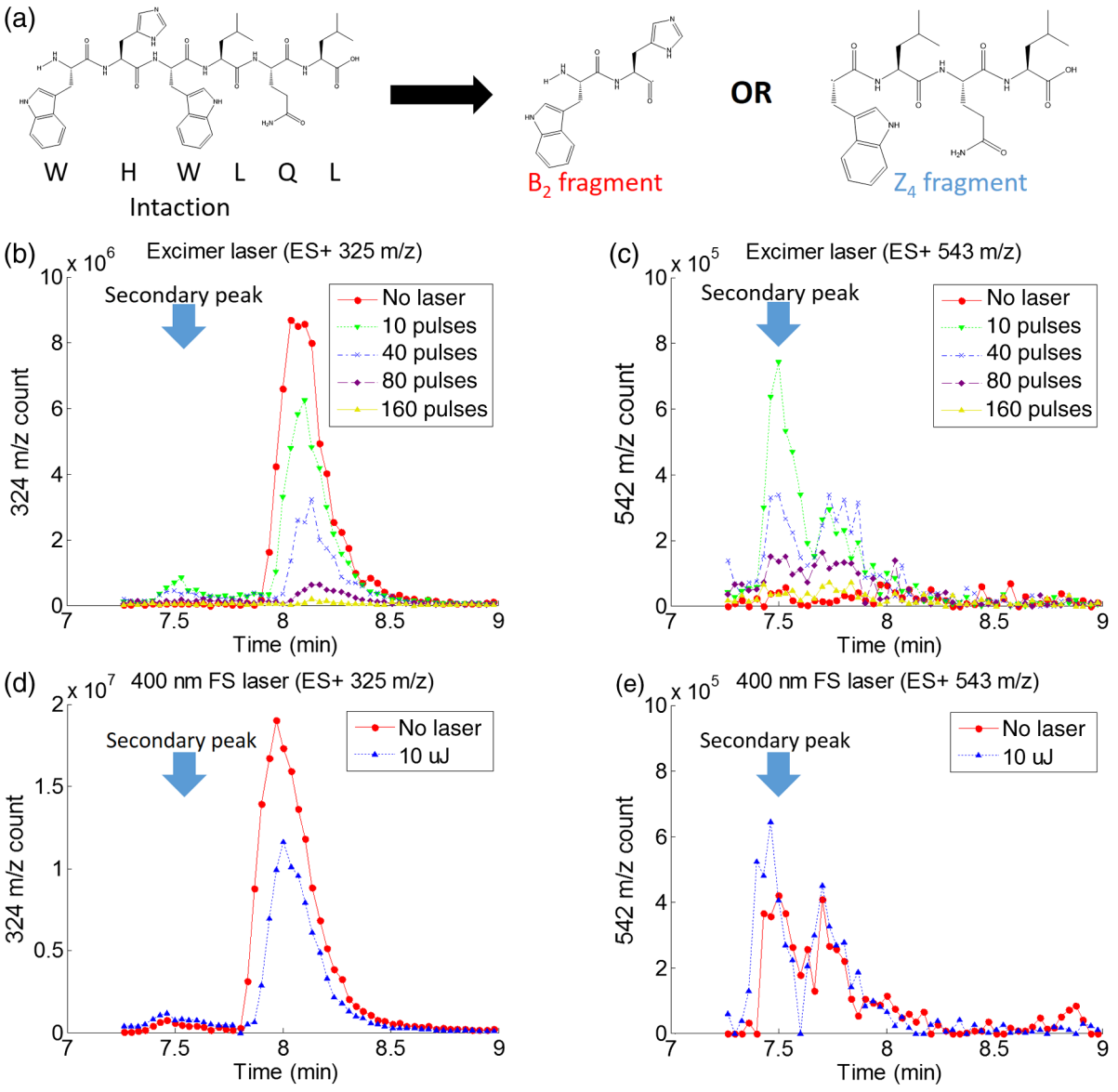

Fig. 7 Photodissociation products after laser irradiation: (a) two possible fragmentation products from intact ion: B_2 fragment with molecular weight (MW) of 324 and Z_4 fragment with 542 MW; (b) chromatogram of 325-m/z channel after excimer laser irradiation. Secondary peak at 7.5 min shows appearance of excimer laser-induced B_2 fragment at 10 laser pulses and disappearance with increasing number of laser pulses; (c) chromatogram of 543-m/z channel after excimer laser irradiation showing appearance of excimer laser-induced Z_4 fragment; (d) chromatogram of 325-m/z channel after 400-nm femtosecond laser irradiation; and (e) chromatogram of 543-m/z channel after 400-nm femtosecond laser irradiation.

bottom row. The familiar microgroove pattern is visible in Figs. 9(b) and 9(d) for 600 and 60 nJ, respectively. Figure 9(e) shows the unsplit lens capsule where the pulse energy of 42 nJ was insufficient for a cut. However, the whiter line along the laser scanning pattern, shown by the arrows, indicates some changes in the tissue.

The summary of the 400-nm femtosecond laser cutting of lens capsule on 13 samples is shown in Fig. 10. The aggregated bubble thresholds are shown in a box-and-whisker plot in Fig. 10(a), with a median value of 66 nJ. The probability of cutting as a function of the pulse energy normalized to the cavitation threshold measured in the specific lens capsule sample is shown in Fig. 10(b). No continuous cuts were made at energies less than 88% of the bubble threshold and the median cutting energy calculated from the probit fit is 93% of the bubble threshold.

4 Discussion

4.1 *Laser-Induced Photodissociation*

Ultrafast lasers have been known to produce photochemical effects without cavitation bubble formation. For instance, the dielectric breakdown produced by femtosecond near-IR lasers resulted in the formation of reactive oxygen species, which led to significant cytotoxicity in mammalian cells.[31] We hypothesized that the photochemical interaction between the ultrafast

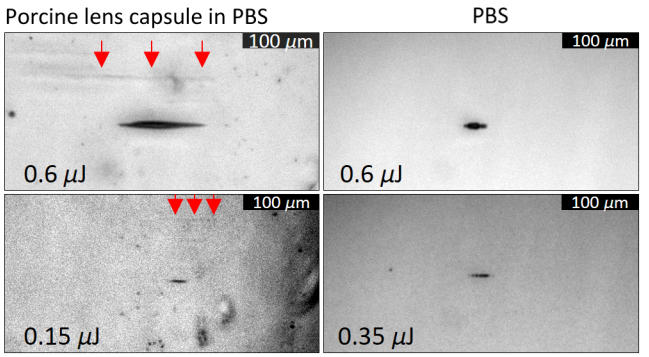

Fig. 8 Flash photography images of cavitation bubbles forming 0.5 μs after laser pulse in lens capsule or in phosphate buffered saline. Arrows indicate cuts in lens capsule from previous laser pulses.

laser and proteins, similar to that which occurs with excimer lasers, could result in dissociation of the proteins and weakening of the lens capsule. Since the lens capsule is under tension, such weakening could be sufficient for splitting the capsule along the line of irradiation. This would also explain why such dense spot spacing was required to complete a cut in the lens capsule at the very low pulse energies.

We explored this hypothesis by first looking for evidence of protein breakdown induced by 400- and 800-nm femtosecond laser pulses, and compared it to the protein breakdown induced by the ArF 193-nm laser. Our results with gel electrophoresis and MS show that 400-nm femtosecond pulses can break protein molecules even below the threshold of cavitation. Unlike the excimer laser though, the process is not linear and thus is confined to the focal volume. In contrast, the 800-nm femtosecond laser pulses show negligible direct interaction with proteins, even above the cavitation threshold, as shown in Fig. 5(a). This indicates that protein dissociation is not merely plasma-mediated photochemistry, and supports the idea of direct multi-photon interaction of the 400-nm femtosecond laser with proteins and peptides.

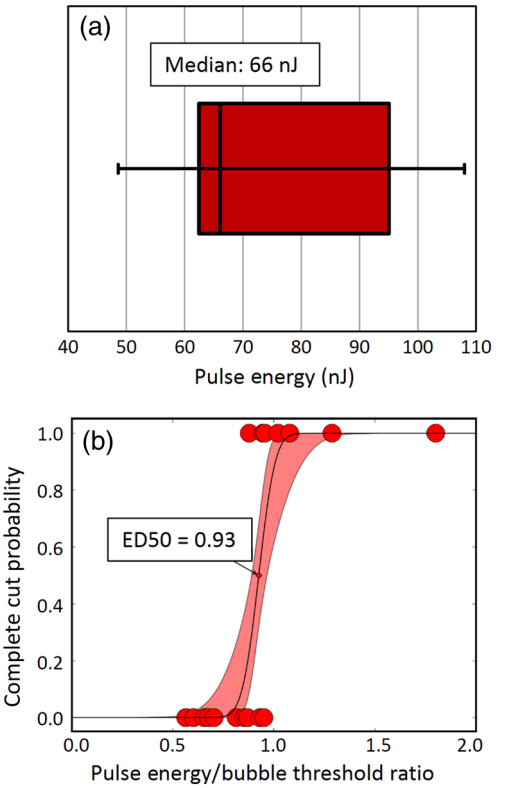

Fig. 10 Threshold energy of extracted lens capsule cutting with 400-nm femtosecond laser: (a) box-and-whisker plot of cavitation bubble threshold in extract porcine lens capsule cutting; and (b) probit plot of complete cut probability with 68% fiducial limits shown as shaded area.

Liquid chromatography and MS analysis provided some insight into the breakdown products from 193- and 400-nm irradiation. Our choice of polypeptide (WHWLQL) was motivated by its water solubility and the presence of several aromatic tryptophan residues, which were shown to have high probability of

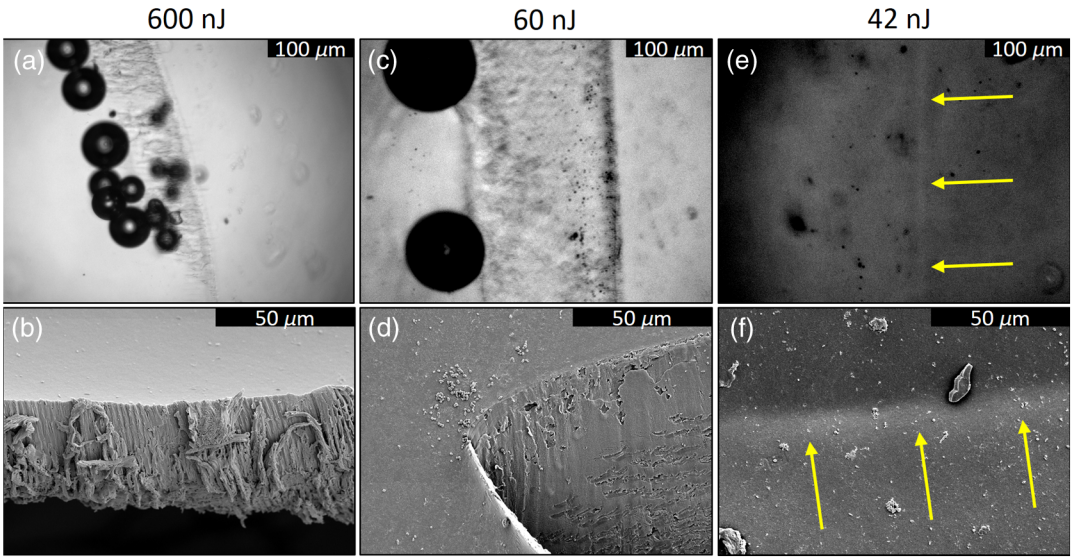

Fig. 9 Cutting of extracted porcine lens capsule pinned to dental wax with 400-nm femtosecond laser. High pulse energy (600 nJ) cut (a) viewed through imaging objective and (b) with SEM on cut edge. Near threshold pulse energy (60 nJ) cut (c) viewed through imaging objective and (d) with SEM on cut edge. Below threshold pulse energy (42 nJ) cut (e) through imaging objective and (f) with SEM on surface.

photochemical damage from 193-nm light by Nikogosyan and Görner.[32] They also demonstrated that the major chromophore for the 193-nm wavelength was the peptide bond itself. The two identifiable breakdown products for 193 nm, shown in Fig. (6), were in fact two fragmentations along the peptide backbone. In contrast, no discernible fragments were seen after 400-nm irradiation, suggesting that the interaction may be less specific to the peptide bond than with 193 nm.

4.2 *Bubble Thresholds and Role of Photodissociation in Tissue Cutting*

To understand the role of photodissociation in low-pulse energy cutting by the 400-nm femtosecond laser, we first needed a reliable determination of cavitation bubble thresholds. A study by Genc et al.[33] showed that biological media, such as minimal essential media and fetal bovine serum, reduced the threshold of cavitation and plasma luminescence for 532-nm, subnanosecond pulses, as compared to distilled water. Given that the lens capsule is acellular and composed mainly of collagen, proteoglycans, and glycoproteins,[34] we used BSA protein as a simple and soluble substitute for the presence of other molecules in the lens capsule. As expected, the addition of BSA to water decreased the cavitation bubble threshold and the effect was much more pronounced with 400 than with 800 nm. At 10 mg/mL of BSA, the ratio between cavitation thresholds with 800- and 400-nm lasers increased from 4 (in water) to 5.8 (with protein). However, protein solutions are limited substitutes for tissue composition, so the determination of bubble threshold in actual lens capsule material was crucial to establishing the role of photodissociation in low-energy tissue dissection.

By simultaneous imaging and cutting of the isolated lens capsule, we were able to directly visualize individual cavitation bubbles and accurately establish the cavitation threshold. This technique also revealed the differences in bubble dynamics between bubbles forming in liquid and in capsule. By varying the LED illumination delay, images of the bubble could be captured at various times after the laser pulse. In water, the laser-induced bubble at low NA is initially elongated but quickly expands into a nearly spherical bubble and collapses equally fast. In tissue, there is only minimal expansion with very little changes in bubble appearance from its initial elongated form, as shown in Fig. 8. This may explain why we had difficulty with very sensitive acoustic detection of the bubble thresholds in tissue.

An important caveat should be noted in comparing absolute thresholds of cutting between the intact lens and the capsule pinned to dental wax. In the former case, the cutting threshold was 2 to 3 times lower primarily since the focusing objective was designed for air. To cut the capsule pinned to dental wax while imaging, the laser focus had to be deeper within the saline solution, which introduced aberrations that increased the threshold energy. To avoid this discrepancy, the data shown in Fig. 9(b) are from lens capsule cutting experiments on the isolated lens capsules with the same amount of saline above the sample as used in the bubble imaging.

These measurements demonstrated that complete cuts are only possible very close to the cavitation threshold in the tissue. The cutting threshold energy, as defined by 50% probability of a successful cut from the probit fit as shown in Fig. 10(b), is 93% of the bubble threshold. Given the high spot density (0.2 μm laterally and 4 μm vertically) and very small difference in the cutting and cavitation thresholds, we conclude that efficient cutting of the lens capsule relies on the usual mechanism of plasma-mediated bubble formation rather than solely on photodissociation.

Like with the 193-nm excimer laser, while there is a measurable photochemical interaction between UV femtosecond lasers and biological molecules, it is not sufficient for tissue cutting. Instead, the finesse of the cut edge with visible femtosecond lasers can be attributed to the lowered cavitation threshold combined with denser spot spacing and a smaller focal volume. Nevertheless, this dissociation of proteins and polypeptides by UV femtosecond lasers below the bubble threshold may prove useful for nonsurgical applications, such as alteration of the refractive index in cornea and lens.[35] It may also damage tissue and produce cytotoxic effects outside the intended focal volume during tissue cutting above the threshold of dielectric breakdown.

4.3 *Lens Capsule Cutting*

The SEM images of porcine lens capsules (Fig. 2) provide a detailed look at how 1030-, 800-, and 400-nm femtosecond lasers cut tissue. Notably, it demonstrates the improved smoothness of the lens capsule edge when moving to a shorter wavelength with correspondingly reduced threshold and focal volume at a given NA. This can be useful for laser capsulotomy since it has been shown that smoother lens capsule edges are more resistant to capsule tears than rougher edges produced by vitrectorhexis.[36]

The capsule edge smoothness is related to the amount of laser energy converted into bubbles. With the 800-nm laser, the bubble threshold was 0.6 μJ, and at this pulse energy, the bubble energy was sufficient for tissue to split even at 1.5-μm spacing. However, at a slightly lower energy of 0.5 μJ, even extremely tight spot spacing of 0.2 μm, corresponding to 20 overlaps (beam diameter/spacing), failed to produce a cut, suggesting that no bubbles were produced. With 400-nm wavelength, the bubble threshold in tissue was as low as 0.02 μJ, and at the threshold, tissue could only be split with very tight spot spacing, 24 overlaps, because very little bubble energy was available to tear the lens capsule. Cuts with these low-energy, tightly spaced bubbles produce smoother capsule edges.

Increasing the spot density above the minimum required for cutting might result in irregular edges, as shown in Fig. 3(c). This is likely due to irregular interactions of the laser with craters formed by the previous pulses. With less dense spacing, each pulse has a more consistent effect, resulting in a more regular pattern of grooves.

Two potential roadblocks for the practical application of UV femtosecond lasers at low NA are the issues of self-focusing and increased scattering. The threshold for self-focusing is described by a critical power, which is proportional to λ^2. Self-focusing in water at 400 nm with $\tau = 150$ fs is expected to occur at pulse energies above 45 nJ. With the median bubble threshold in water of 121 nJ for 400 nm at low NA, this could interfere with accurate cutting.

A working system could be implemented with slightly longer pulses since the critical energy of self-focusing increases linearly with pulse duration, while the increase in threshold of dielectric breakdown is less than linear in this range. For instance, Hammer et al.[37] measured laser-induced breakdown thresholds in water of 1.92 μJ for 400 fs and 1.31 μJ for 100 fs, a factor of less than 1.5. With 600-fs pulses, the critical energy of self-focusing would be 180 nJ for 400-nm

wavelength, and if the dielectric breakdown threshold would increase by less than a factor of 1.5, compared to 150-fs pulses ($E = 121$ nJ in water), self-focusing effects could be avoided.

An UV femtosecond laser would also have to contend with increased scattering in ocular media for the shorter wavelength. According to Boettner and Wolter,[38] direct transmission through the cornea at 400 nm is ~40%. Our measurements indicate that bubble thresholds in the lens capsule are about half the water thresholds, which are close to what is needed to compensate for the scattering losses. These issues would need to be carefully investigated if UV lasers are to be used for capsulotomy or other applications deep in the eye.

5 Conclusions

A comparison of lens capsule cutting with femtosecond lasers at UV (400 nm) and near-IR (800 and 1030 nm) wavelengths demonstrates that UV lasers are capable of remarkably smooth cuts. Analysis of the interaction with proteins and polypeptides shows that UV femtosecond lasers induce significant photodissociation of proteins and polypeptides in a multiphoton regime, while IR lasers do not. Nevertheless, careful measurement of the bubble thresholds and cutting thresholds reveals that cutting of tissue with the UV femtosecond laser is the result of plasma-mediated bubble formation, but with thresholds lowered by the presence of biological molecules. Low thresholds, tight spot spacing, and smaller focal volume for a given focusing geometry combine to produce very smooth cut tissue edges.

Acknowledgments

We would like to thank Dimitri Simanovskii for his aid in setting up the laser system, Alexander Vankov for discussions on laser-tissue interactions, and Philip Huie and Roopa Dalal for their help with tissue sample preparation. We are grateful for the funding provided by the U.S. Air Force Office of Scientific Research (Grant No. FA9550-10-1-0503) and the Stanford Photonics Research Center.

References

1. D. Aron-Rosa et al., "Use of the neodymium-YAG laser to open the posterior capsule after lens implant surgery: a preliminary report," *J. Am. Intraocul. Implant Soc.* **6**(4), 352–354 (1980).
2. S. L. Trokel, R. Srinivasan, and B. Braren, "Excimer laser surgery of the cornea," *Am. J. Ophthalmol.* **96**(6), 710–715 (1983).
3. I. Ratkay-Traub et al., "First clinical results with the femtosecond neodymium-glass laser in refractive surgery," *J. Refractive Surg.* **19**(2), 94–103 (2003).
4. Z. Nagy et al., "Initial clinical evaluation of an intraocular femtosecond laser in cataract surgery," *J. Refractive Surg.* **25**(12), 1053–1060 (2009).
5. D. V. Palanker et al., "Femtosecond laser-assisted cataract surgery with integrated optical coherence tomography," *Sci. Transl. Med.* **2**(58), 58ra85 (2010).
6. B. J. Garrison and R. Srinivasan, "Laser ablation of organic polymers: microscopic models for photochemical and thermal processes," *J. Appl. Phys.* **57**(8), 2909–2914 (1985).
7. R. Srinivasan and W. J. Leigh, "Ablative photodecomposition: action of far-ultraviolet (193 nm) laser radiation on poly(ethylene terephthalate) films," *J. Am. Chem. Soc.* **104**(24), 6784–6785 (1982).
8. J. M. Isner and R. H. Clarke, "The paradox of thermal ablation without thermal injury," *Lasers Med. Sci.* **2**(3), 165–173 (1987).
9. W. B. Telfair et al., "Histological comparison of corneal ablation with Er:YAG laser, Nd:YAG optical parametric oscillator, and excimer laser," *J. Refractive Surg.* **16**(1), 40–50 (2000).
10. N. Bityurin et al., "Models for laser ablation of polymers," *Chem. Rev.* **103**(2), 519–552 (2003).
11. A. Vogel and V. Venugopalan, "Mechanisms of pulsed laser ablation of biological tissues," *Chem. Rev.* **103**(2), 577–644 (2003).
12. T. Lippert and J. T. Dickinson, "Chemical and spectroscopic aspects of polymer ablation: special features and novel directions," *Chem. Rev.* **103**(2), 453–485 (2003).
13. M. Kitai et al., "The physics of UV laser cornea ablation," *IEEE J. Quantum Electron.* **27**(2), 302–307 (1991).
14. A. Vogel et al., "Mechanisms of femtosecond laser nanosurgery of cells and tissues," *Appl. Phys. B* **81**(8), 1015–1047 (2005).
15. N. Linz et al., "Wavelength dependence of nanosecond infrared laser-induced breakdown in water: evidence for multiphoton initiation via an intermediate state," *Phys. Rev. B* **91**(13), 1–10 (2015).
16. A. Vogel et al., "Controlled nonlinear energy deposition in transparent materials: experiments and theory," *AIP Conf. Proc.* **51**, 51–55 (2010).
17. M. J. Pollhammer et al., "Refractive surgery with a new UV-femtosecond laser: safety profile and basic considerations," *Invest. Ophthalmol. Visual Sci.* **49**(13), 3359 (2008).
18. R. Le Harzic et al., "Ultraviolet femtosecond laser creation of corneal flap," *J. Refractive Surg.* **25**(4), 383–389 (2009).
19. C. M. Hammer et al., "Corneal tissue interactions of a new 345 nm ultraviolet femtosecond laser," *J. Cataract Refractive Surg.* **41**(6), 1279–1288 (2015).
20. A. Trost et al., "A new nanosecond UV laser at 355 nm: early results of corneal flap cutting in a rabbit model," *Invest. Ophthalmol. Visual Sci.* **54**(13), 7854–7864 (2013).
21. C. Crotti et al., "Wavelength optimization in femtosecond laser corneal surgery," *Invest. Ophthalmol. Visual Sci.* **54**(5), 3340–3349 (2013).
22. L. Ding et al., "Intratissue refractive index shaping (IRIS) of the cornea and lens using a low-pulse-energy femtosecond laser oscillator," *Invest. Ophthalmol. Visual Sci.* **49**(12), 5332–5339 (2008).
23. L. Xu, W. H. Knox, and K. R. Huxlin, "Exogenous and endogenous two-photon absorption for intra-tissue refractive index shaping (IRIS) in live corneal tissue [Invited]," *Opt. Mater. Express* **1**(7), 1159 (2011).
24. Y. Guo et al., "Femtosecond laser collagen cross-linking without traditional photosensitizers," *Proc. SPIE* **9321**, 932103 (2015).
25. N. J. Friedman et al., "Femtosecond laser capsulotomy," *J. Cataract Refractive Surg.* **37**(7), 1189–1198 (2011).
26. S. Serrao et al., "Analysis of femtosecond laser assisted capsulotomy cutting edges and manual capsulorhexis using environmental scanning electron microscopy," *J. Ophthalmol.* **2014**, 1–7 (2014).
27. W. J. Mayer et al., "Cell death and ultrastructural morphology of femtosecond laser-assisted anterior capsulotomy," *Invest. Ophthalmol. Visual Sci.* **55**(2), 893–898 (2014).
28. T. Kohnen et al., "Morphological changes in the edge structures following femtosecond laser capsulotomy with varied patient interfaces and different energy settings," *Graefes Arch. Clin. Exp. Ophthalmol.* **252**(2), 293–298 (2014).
29. J. Zhang et al., "Second-harmonic generation from regeneratively amplified femtosecond laser pulses in BBO and LBO crystals," *J. Opt. Soc. Am. B* **15**(1), 200 (1998).
30. I. Toytman et al., "Multifocal laser surgery: cutting enhancement by hydrodynamic interactions between cavitation bubbles," *Phys. Rev. E* **82**(4), 046313 (2010).
31. U. K. Tirlapur et al., "Femtosecond near-infrared laser pulses elicit generation of reactive oxygen species in mammalian cells leading to apoptosis-like death," *Exp. Cell Res.* **263**(1), 88–97 (2001).
32. D. N. Nikogosyan and H. Görner, "Laser-induced photodecomposition of amino acids and peptides: extrapolation to corneal collagen," *IEEE J. Sel. Top. Quantum Electron.* **5**(4), 1107–1115 (1999).
33. S. L. Genc, H. Ma, and V. Venugopalan, "Low-density plasma formation in aqueous biological media using sub-nanosecond laser pulses," *Appl. Phys. Lett.* **105**(6), 063701 (2014).
34. B. P. Danysh and M. K. Duncan, "The lens capsule," *Exp. Eye Res.* **88**(2), 151–164 (2009).
35. L. Xu et al., "Noninvasive intratissue refractive index shaping (IRIS) of the cornea with blue femtosecond laser light," *Invest. Ophthalmol. Visual Sci.* **52**(11), 8148–8155 (2011).
36. L. K. Andreo, M. E. Wilson, and D. J. Apple, "Elastic properties and scanning electron microscopic appearance of manual continuous curvilinear capsulorhexis and vitrectorhexis in an animal model of pediatric cataract," *J. Cataract Refractive Surg.* **25**(4), 534–539 (1999).

37. D. X. Hammer et al., "Experimental investigation of ultrashort pulse laser-induced breakdown thresholds in aqueous media," *IEEE J. Quantum Electron.* **32**(4), 670 (1996).
38. E. Boettner and J. Wolter, "Transmission of the ocular media," *Invest. Ophthalmol. Visual Sci.* **1**(6), 776–783 (1962).

Jenny Wang received her AB degree in chemistry and physics from Harvard College in 2010. She is currently pursuing a PhD in applied physics from Stanford University, working on laser-tissue interactions in ophthalmic surgery.

Georg Schuele: Biography is not available.

Daniel Palanker is a professor in the Department of Ophthalmology and in the Hansen Experimental Physics Laboratory at Stanford University. He is working on optical and electronic technologies for imaging, diagnostic, therapeutic, surgical, and prosthetic applications, primarily in ophthalmology. These studies include laser-tissue interactions with applications to nondamaging laser therapy and surgery with ultrafast lasers, retinal prosthetics for restoration of sight, electronic control of organs, as well as interferometric imaging of neural signals.